Energy balance in nanosecond pulse discharges in nitrogen and air

Ivan Shkurenkov and Igor V Adamovich

Nonequilibrium Thermodynamics Laboratory, Department of Mechanical and Aerospace Engineering, The Ohio State University, Columbus, OH 43210, USA

E-mail: adamovich.1@osu.edu

Abstract

Kinetic modeling is used to analyze energy partition and energy transfer in nanosecond pulse discharges sustained between two spherical electrodes in nitrogen and air. The modeling predictions are compared with previous time-resolved temperature and $N_2(X\ ^1\Sigma_g^+, v = 0-9)$ vibrational population measurements by picosecond broadband coherent anti-Stokes Raman spectroscopy (CARS) and phase-locked Schlieren imaging. The model shows good agreement with experimental data, reproducing experimental discharge current pulse waveforms, as well as dominant processes of energy transfer in the discharge and the afterglow. Specifically, the results demonstrate that the temperature rise in the plasma occurs in two stages, (i) 'rapid' heating on sub-acoustic time scale, dominated by $N_2(A\ ^3\Sigma_u^+)$ energy pooling processes, $N_2(B^3\Pi_g)$ and $N(^2P, ^2D)$ quenching (in nitrogen), and by quenching of excited electronic states of N_2 molecules by O_2 (in air), and (ii) 'slow' heating due to N_2 vibrational relaxation by O atoms (in air), nearly completely missing in nitrogen. Comparison of the model predictions with N_2 vibrational level populations confirms that the N_2 vibrational temperature rises after the discharge pulse is caused by the 'downward' vibrational–vibrational exchange depopulating higher vibrational levels and populating vibrational level $v = 1$. The model reproduces temporal dynamics of vibrational level populations and temperature in the discharge and the afterglow, indicating that energy partition among different modes (vibrational, electronic, dissociation, and ionization) is predicted accurately. At the present conditions, energy fraction coupled to the positive column of the discharge filament in air is approximately 50%, with the rest coupled to the cathode layer. Nearly 10% of the total pulse energy is spent on O atom generation, and about 10% is thermalized on a sub-acoustic time scale, producing a strong compression wave in the radial direction. The experimental wave speed is considerably higher compared to the model predictions, by approximately 30%. The reason for this difference may be due to interaction between the cylindrical and spherical compression waves generated in the discharge filament and in the cathode layer, respectively.

Keyword:nanosecond discharge, rapid heating, vibrational relaxation

(Some figures may appear in colour only in the online journal)

1. Introduction

Kinetics of vibrational and electronic energy transfer, temperature rise, and chemical reactions in nitrogen and air plasmas sustained by ns pulse discharges has been extensively studied over the last decade. Time-resolved measurements of temperature [1–5], absolute populations of excited electronic states of N_2 [2, 3], absolute number densities of O atoms [2, 3], N atoms and NO [6], and vibrational level populations of ground electronic state N_2 and O_2 [6–10], as well as detection of compression wave formation [11, 12] in these discharges generated significant amount of data to provide insight into dominant energy transfer processes and chemical reactions in these highly nonequilibrium plasmas and afterglow. This
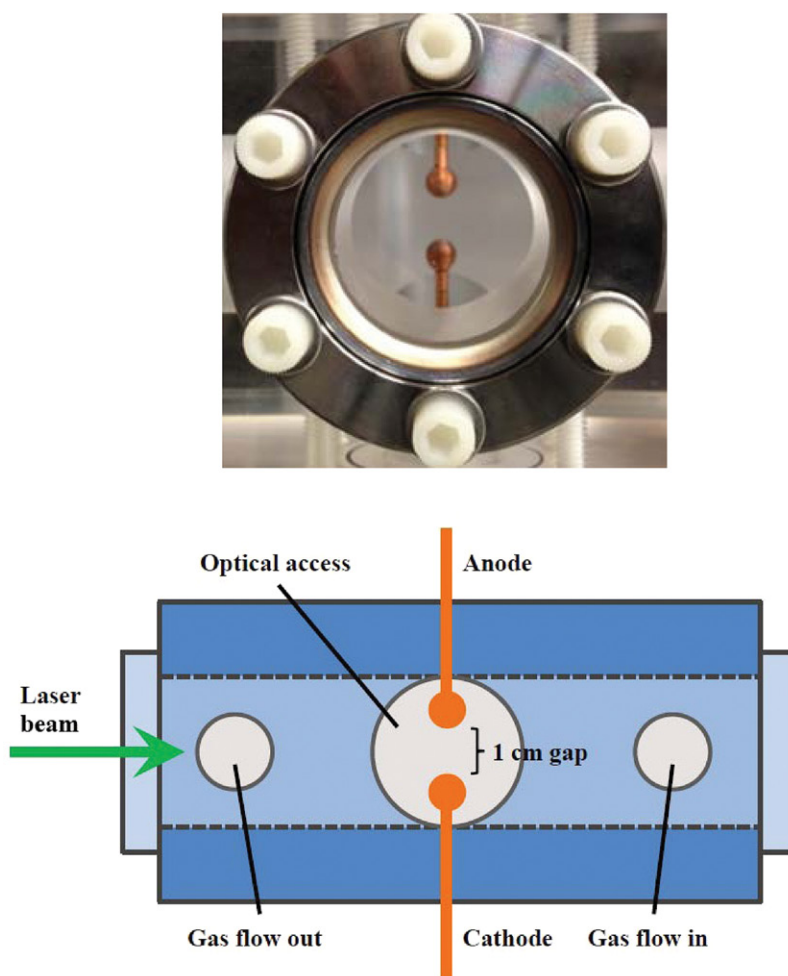
Figure 1. Photograph and schematic of the discharge cell.

insight makes possible effective use of ns pulse discharges for a number of applications, including high-speed flow control [13, 14] (based on rapid energy thermalization in a discharge, on a time scale shorter than the acoustic time scale), plasma assisted combustion [15], and plasma biomedicine [16] (both based on efficient generation of excited species and chemically active radicals).

In spite of a growing body of experimental data, kinetic modeling of these discharges, incorporating state-specific energy transfer processes at high specific energy loading and in realistic geometry, is still under development. Recent work at Moscow State University [17, 18], CNRS [19], Ecole Centrale Paris [19–21], Georgia Tech [22], Tohoku University [23], and Ohio State University [5, 24] advanced this field considerably. However, modeling predictions of the experimental results, in particular of experiments with time-resolved measurements of temperature, pressure, vibrational level populations, and species number densities [7–10] require significant additional effort. The main objective of the present work is to use the kinetic model developed and validated in our previous work [5, 24] to predict time-resolved N_2 vibrational level populations, temperature, and pressure during and after a single filament ns pulse discharge in nitrogen and air, compare the modeling prediction with experimental results [10, 12], and determine energy balance in this type of the discharge.

2. Experimental

The experiments modeled in the present work are discussed in detail in our previous publications [10, 12]. Briefly, the experiments were done in a four-arm cross glass cell with quartz windows, with two spherical copper electrodes 7.5 mm in diameter and separated by a 10 mm gap placed in the cell, as shown in figure 1. A nanosecond pulse, diffuse filament discharge in 100 Torr of nitrogen or dry air was sustained between the electrodes by a custom-made pulsed plasma generator producing 10 kV peak voltage pulses ~100 ns duration, at a low pulse repetition rate of $\nu = 50$ Hz. The flow velocity in the cell, estimated from the flow rate, ~0.25 m s^{-1}, corresponds to flow residence time of approximately 20 ms, such that the flow in the cell experiences only ~1–2 discharge pulses. Typical voltage, current, and coupled energy waveforms in the discharge in air are shown in figure 2, both for the 'main' discharge pulse and for the weak 'after-pulse' discharge, produced by the plasma generator approximately 500 ns after the main pulse. The 'after-pulse' is an artifact of the output of the custom-designed high-voltage pulse generator used in the present work. The main advantage of using this power supply compared to commercial pulse generators is high energy coupled per pulse, up to 15–20 mJ, which results in significant rapid heating and vibrational nonequilibrium at
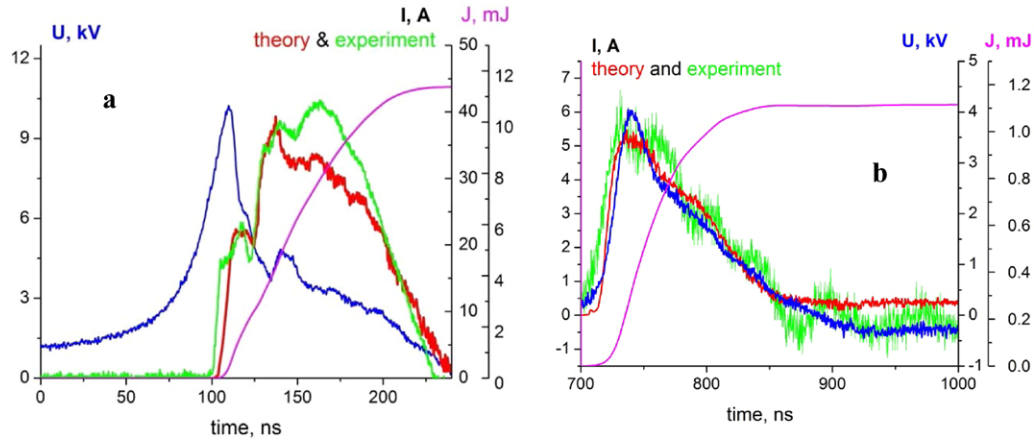
Figure 2. Voltage (experimental), current (experimental and predicted), and coupled energy (predicted) waveforms during the main pulse (a) and during the 'after-pulse' (b) in air at $P = 100$ Torr.

the present conditions. Discharge pulse waveforms in nitrogen are very similar to the ones for air. At these conditions, total energy coupled to the plasma is approximately 13 mJ/pulse in nitrogen and approximately 16 mJ in air. It can be seen that the main pulse couples approximately 90% of the energy to the plasma (see figure 2). Figure 3 shows single-shot ICCD images of the main pulse and of the after-pulse taken using a 100 ns camera gate, indicating partial contraction of the discharge filament during the after-pulse. In both images, the bottom electrode is grounded. The diameter of the filament generated during the main pulse is approximately 2.0 mm (FWHM of emission intensity radial distribution).

Time-resolved temperature and $N_2(v = 0–9)$ vibrational level populations in the discharge and in the afterglow (on the discharge filament centerline) were measured by picosecond broadband vibrational coherent Anti-Stokes Raman scattering (CARS) in BOXCARS phase matching geometry, with spatial resolution (interaction length in the direction of laser beams) of 0.5 mm [10]. Translational/rotational temperature was inferred from partially rotationally resolved vibrational CARS spectra (Q-branch of $v = 1 \rightarrow 0$ band) using CARSFIT synthetic spectrum code. Compression waves generated due to rapid heating of the gas in the discharge filament were detected using a custom-built phase-locked Schlieren system [12]. These measurements are discussed in greater detail in the original papers [10, 12].

3. Kinetic model

The kinetic model used to study energy transfer in the nanosecond pulse discharge between the electrodes and in the afterglow, as well as the effect on the gas mixture in the cell is described in detail in our recent work [5, 24]. Briefly, the discharge pulse is modeled using a 1D axial model, with the coordinate axis directed along the filament centerline, and the afterglow is modeled using a 1D radial axisymmetric model. The axial model incorporates Poisson equation for the axial electric field, Boltzmann equation for plasma electrons in two-term approximation including electron–electron collisions, equation for the electron temperature, time-dependent conservation equations for number densities of charged
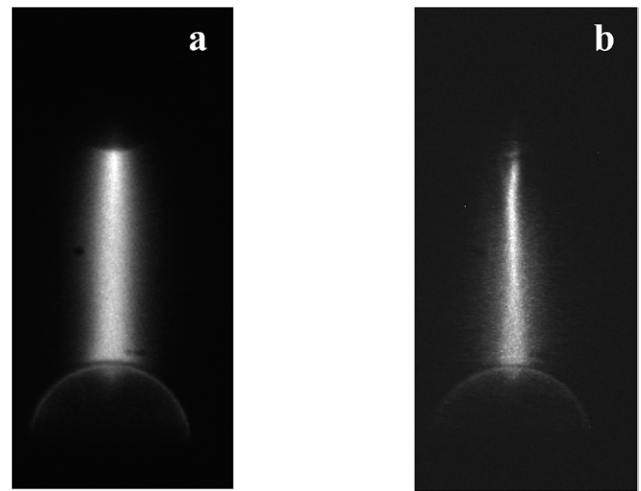
Figure 3. ICCD images of plasmas generated in air during the main pulse (a) and during the 'after-pulse' 500 ns later (b). $P = 100$ Torr, camera gate 100 ns, bottom electrode is grounded.

species (electrons, positive ions, and negative ions) and neutral species (including excited electronic states of N_2, O_2, N, and O), equations for relative populations of N_2 vibrational levels ('master equation'), and heavy species energy equation. The model used the experimental voltage waveform, such as shown in figure 2, as input. In the present work, kinetics of energy transfer during collisional quenching of excited electronic states of N_2 molecules and N atoms has been revised, to account for partial energy storage in the vibrational energy mode of the ground electronic state of N_2 [25]. Without this revision, the model would predict considerably more rapid temperature rise in the discharge and afterglow in nitrogen, at variance with the experimental results [10]. The list of quenching processes of N_2 and N species and their rate coefficients, used in the present model, is given in table 1. Note that according to a recent study [26], kinetics of energy transfer among excited vibrational and electronic levels of nitrogen molecules may be strongly coupled to vibrational excitation of nitrogen molecules in the metastable $A\,^3\Sigma_u^+$ state. However, incorporating vibrationally excited molecules $N_2(A\,^3\Sigma_u^+, v)$ into the kinetic model would require knowledge of a significant

Table 1. List of N_2 and N quenching processes and their rate coefficients.

	Process	Rate coefficient $(cm^3 \, s^{-1})$	Energy defect (eV)	Ref.
(R1)	$N_2(A\,^3\Sigma_u^+) + N_2(A\,^3\Sigma_u^+) \rightarrow N_2(B^3\Pi_g) + N_2(X\,^1\Sigma_g^+, v = 12)$	7.7×10^{-11}	1.76	[25]
(R2)	$N_2(A\,^3\Sigma_u^+) + N_2(A\,^3\Sigma_u^+) \rightarrow N_2(C^3\Pi_u) + N_2(X\,^1\Sigma_g^+, v = 4)$	1.5×10^{-10}	0.18	[25]
(R3)	$N_2(A\,^3\Sigma_u^+) + N(^4S) \rightarrow N_2(X\,^1\Sigma_g^+, 6 \leqslant v \leqslant 9) + N(^2P)$	4.4×10^{-11}	0.91–0.12	[27]
(R4)	$N_2(a'\,^1\Sigma_u^-) + N_2 \rightarrow N_2(B^3\Pi_g) + N_2$	1.9×10^{-13}	0.24	[26]
(R5)	$N_2(a\,^1\Pi_g) + N_2 \rightarrow N_2(a'\,^1\Sigma_u^-) + N_2$	2×10^{-11}	0.15	[26]
(R6)	$N_2(w^1\Delta_u) + N_2 \rightarrow N_2(a\,^1\Pi_g) + N_2$	10^{-11}	0.34	[26]
(R7)	$N_2(a''\,^1\Sigma_g^+) + N_2 \rightarrow N_2(a\,^1\Pi_g) + N_2$	3×10^{-13}	3.7	[26]
(R8)	$N(^4S) + N(^4S) + N_2 \rightarrow N_2(B^3\Pi_g) + N_2$	$8.27 \times 10^{-34} \cdot \exp(500/T)$	2.44	[26]
(R9)	$N(^2D) + N_2 \rightarrow N(^4S) + N_2$	$4.52 \times 10^{-14} \times T^{0.68} \cdot \exp(-1438/T)$	2.8	[28]
(R10)	$N(^2P) + N(^4S) \rightarrow N(^4S) + N(^2D)$	6×10^{-13}	1.2	[25]
(R11)	$N(^2P) + N(^4S) \rightarrow N(^4S) + N(^4S)$	1.8×10^{-12}	3.58	[25]
(R12)	$N(^2P) + N_2 \rightarrow N(^4S) + N_2$	3×10^{-17}	3.58	[27]
(R13)	$N_2(B^3\Pi_g) + N_2 \rightarrow N_2(A\,^3\Sigma_u^+) + N_2(X\,^1\Sigma_g^+, v = 4)$	2.85×10^{-11}	0.86	[25]
(R14)	$N_2(W^3\Delta_u) + N_2 \rightarrow N_2(A\,^3\Sigma_u^+) + N_2(X\,^1\Sigma_g^+, v = 4)$	2.85×10^{-11}	0.06	[25]
(R15)	$N_2(B'\,^3\Sigma_u^-) + N_2 \rightarrow N_2(A\,^3\Sigma_u^+) + N_2(X\,^1\Sigma_g^+, v = 7)$	2.85×10^{-11}	0.04	[25]
(R16)	$N_2(B^3\Pi_g) + N_2 \rightarrow N_2(X\,^1\Sigma_g^+) + N_2$	1.5×10^{-12}	7.35	[25]
(R17)	$N_2(W^3\Delta_u) + N_2 \rightarrow N_2(X\,^1\Sigma_g^+) + N_2$	1.5×10^{-12}	7.36	[25]
(R18)	$N_2(B'\,^3\Sigma_u^-) + N_2 \rightarrow N_2(X\,^1\Sigma_g^+) + N_2$	1.5×10^{-12}	8.16	[25]
(R19)	$N_2(C^3\Pi_u) + N_2 \rightarrow N_2(B^3\Pi_g) + N_2(X\,^1\Sigma_g^+, v = 13)$	3.85×10^{-12}	0.21	[25]
(R20)	$N_2(E\,^3\Sigma_g^+) + N_2 \rightarrow N_2(B^3\Pi_g) + N_2(X\,^1\Sigma_g^+, v = 17)$	3.85×10^{-12}	0.11	[25]

number of state-specific vibrational/electronic energy transfer rates, which are not available.

The initial radial distributions of species number densities at the end of the discharge pulse (when the applied voltage falls to zero, at $t = 100$ ns), used by the radial model, are assumed to follow experimental broadband plasma emission intensity halfway between the electrodes, approximated as a Gaussian distribution with FWHM of 2.0 mm. The radial model incorporates time-dependent compressible Navier–Stokes equations for conservation of mass, momentum, energy, species concentrations, and master equation for N_2 vibrational level populations [5]. Both Poisson equation and Boltzmann equation are disabled during the afterglow. The main objective of the radial model is to predict evolution of temperature and pressure in the discharge filament, controlled by rapid heating in the plasma (on the time scale shorter than the acoustic time scale), and propagation of a resultant compression wave in the radial direction. The modeling calculations were carried out in nitrogen and dry air, at $P = 100$ Torr.

The use of the present approach is justified in the entire discharge gap, except in the cathode layer region, where the compression wave becomes non-1D [12]. The present approach offers a low computational cost alternative to 2D models of transient high-pressure nonequilibrium electric discharges in compressible molecular gases. The present model is considerably more accurate compared to a 0D kinetic model used in [10], where electric field and electron density in the plasma were estimated from experimental voltage and current waveforms.

4. Results and discussion

Figure 2, which plots experimental discharge voltage, current, and coupled energy waveforms for the main pulse and the after-pulse in air, also shows the predicted current pulse waveforms, illustrating the good agreement between the model predictions and the data. As in our previous work [5], current density predicted by the 1D axial model was multiplied by the discharge filament cross sectional area based on the FWHM diameter inferred from the radial distribution of plasma emission halfway between the electrodes (see figure 3), 2.0 mm and 0.67 mm, respectively. Since the peak voltage and current during the after-pulse are significantly lower compared to the main pulse (see figure 2), energy coupling to the plasma during the after-pulse is also much lower, 1.15 mJ versus 13.3 mJ. However, specific energy loading during the after-pulse may be fairly significant since it occurs in a partially constricted discharge filament (see figure 3).

Figure 4(a) compares the experimental and predicted temperature during and after the discharge pulse in nitrogen, plotted together with predicted rates of energy dissipation in different energy transfer processes. In figure 4, $t = 0$ corresponds to the beginning of the main pulse current rise. It can be seen that on sub-μs time scale, up to $t \approx 2\,\mu$s, the two dominant processes controlling the temperature rise in the discharge and in the afterglow are the energy pooling reaction, (R1)

$$N_2(A\,^3\Sigma_u^+) + N_2(A\,^3\Sigma_u^+) \rightarrow N_2(B\,^3\Pi_g) + N_2(X\,^1\Sigma_g^+, v = 8), \tag{1}$$
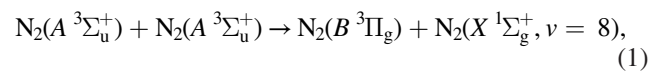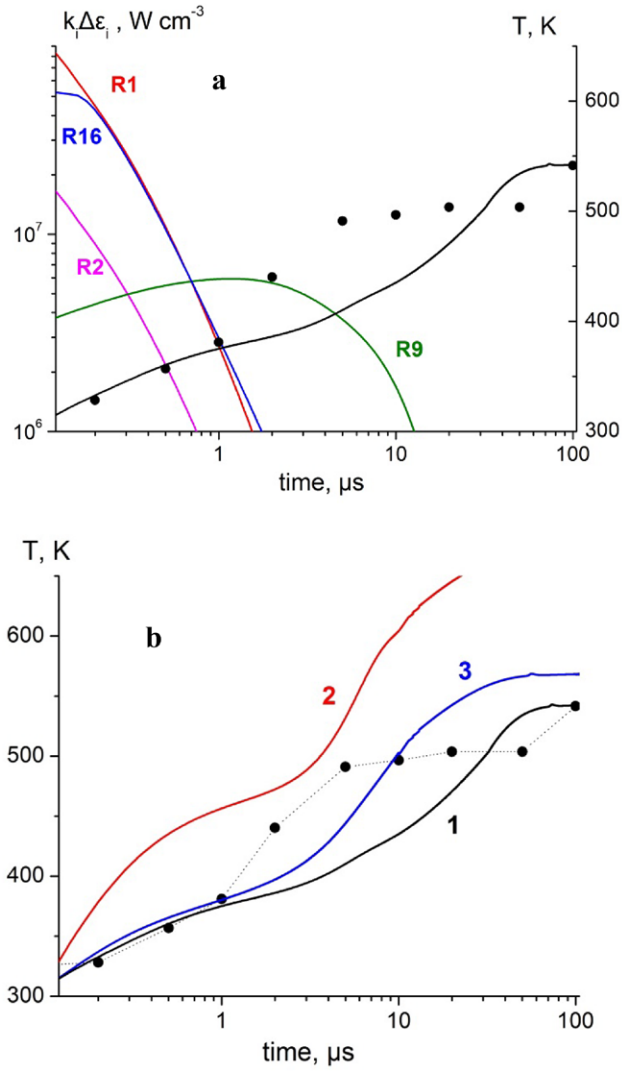
Figure 4. (a) Time-resolved gas temperature during and after the discharge pulse in nitrogen predicted by the model, plotted together with predicted rates of energy dissipation in dominant energy transfer processes; (b) comparison of model predictions with experimental data using three different assumptions (see details in the text). Symbols: experimental data, lines: model predictions.

and quenching of the $B\,{}^3\Pi$ state of N_2 to the ground electronic state, reaction (R16)

$$N_2(B\,{}^3\Pi_g) + N_2 \rightarrow N_2(X\,{}^1\Sigma_g^+) + N_2. \tag{2}$$
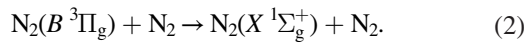
These two processes are mainly responsible for the 'rapid' temperature rise in the plasma on sub-acoustic time scale, $t < \tau_{acoustic} = r/a \sim 3\ \mu s$, where $r \approx 1\,mm$ is the filament radius and $a \approx 350\ m\ s^{-1}$ is the speed of sound. On a longer time scale, $t \sim 3$–$30\ \mu s$, quenching of metastable N atoms,

$$N({}^2P) + N_2 \rightarrow N({}^4S) + N_2, \tag{3}$$

$$N({}^2D) + N_2 \rightarrow N({}^4S) + N_2, \tag{4}$$
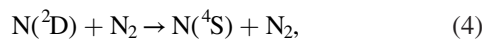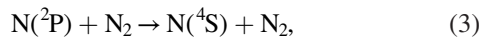
(reactions (R12) and (R9)) also contribute significantly to the 'slow' temperature rise, $t > \tau_{acoustic}$.

Figure 4(b) compares temperature rise in nitrogen predicted by the model with the experimental data, using three different
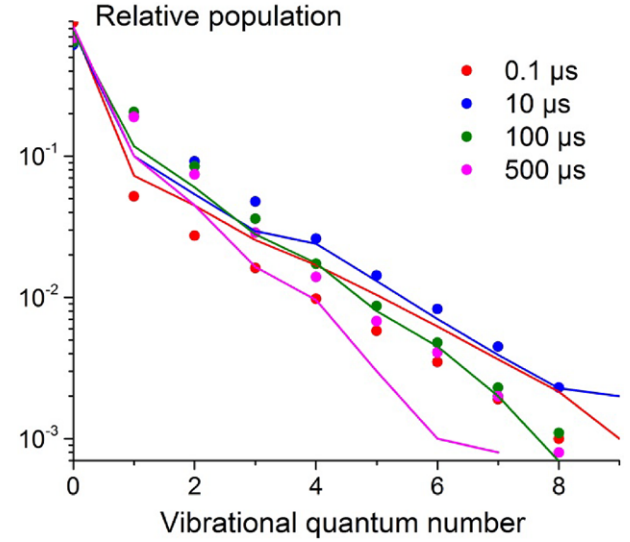
Figure 5. Experimental and predicted N_2 vibrational distribution functions after the discharge pulse in nitrogen, at different delay times after beginning of the main pulse. Symbols: experimental data, lines: model predictions.

assumptions. Line 1 shows temperature rise predicted by the baseline model, using reactions listed in table 1. It can be seen that temperature reaches $T \approx 500\,K$ at $t = 100\ \mu s$, very close to the experimental value. However, temperature rise predicted on a shorter time scale, $t \sim 1$–$10\ \mu s$, is noticeably slower compared to the data. Line 2 shows temperature growth predicted by the model assuming that all energy defect in reactions (R1) and (R2) is thermalized, instead of being stored in the vibrational mode of the ground electronic state of nitrogen, $N_2(X\,{}^1\Sigma_g^+, v)$. In this case, temperature rise on the short time scale, $t \sim 0.1$–$1\ \mu s$, is much faster compared to the data, illustrating that not accounting for ground state vibrational excitation during $N_2(A\,{}^3\Sigma_u^+)$ energy pooling reactions results in significant overprediction of 'rapid' temperature rise in the plasma on sub-microsecond time scale, by approximately a factor of two. Note that since quenching of excited electronic states of N_2 occurs on sub-microsecond time scale at the present conditions, it cannot be the mechanism of significant temperature rise at $t \sim 1$–$10\ \mu s$, detected in the experiment and underpredicted by the baseline model (line 1). However, from figure 4(a), it is evident that quenching of electronically excited N atoms (e.g. reaction (R9)) does occur on the right time scale, and is therefore the most likely kinetic mechanism responsible for the temperature rise at this stage. Electronically excited atoms, $N({}^2P)$ and $N({}^2D)$, may well be generated by electron impact during the discharge pulse. However, to the best of our knowledge, experimental cross sections for these processes are not available. To estimate the effect of excited N atoms on temperature rise at $t \sim 1$–$10\ \mu s$, we assumed that 20% of nitrogen atoms produced during the discharge are generated in $N({}^2D)$ state. Line 3 in figure 4(b) plots temperature evolution predicted by the model using this assumption. Indeed, it can be seen that in this case the model predictions are closer to the experimental data, suggesting that temperature rise in nitrogen afterglow on microsecond time
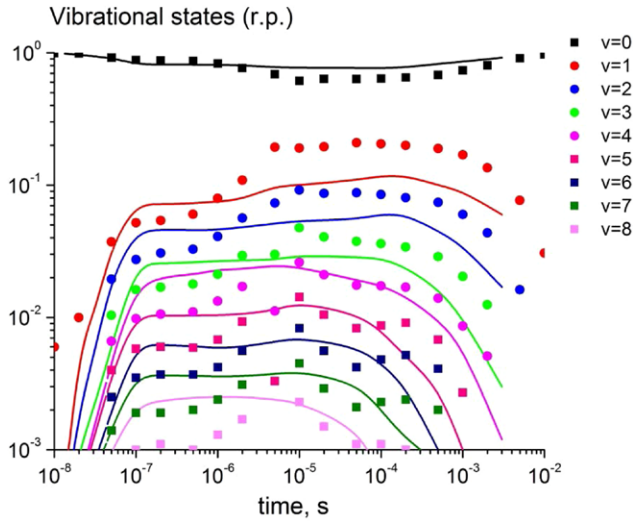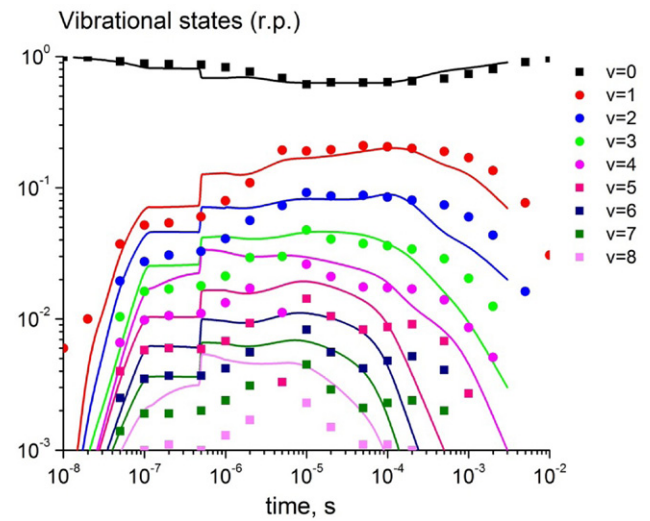
Figure 6. Experimental and predicted $N_2(v = 0-9)$ vibrational level populations, plotted versus time after beginning of the main discharge pulse in nitrogen. Symbols: experimental data, lines: model predictions.

Figure 7. Experimental and predicted $N_2(v = 0-9)$ vibrational level populations, plotted versus time after beginning of the main discharge pulse in nitrogen, with additional energy loading by the after-pulse at $t = 500$ ns taken into account. Symbols: experimental data, lines: model predictions.

scale is controlled by quenching of excited nitrogen atoms produced by the discharge.

Figure 5 plots experimental and predicted vibrational level populations of the ground electronic state of nitrogen, $N_2(X \ ^1\Sigma_g^+, v)$, at different delay times after the beginning of the main discharge pulse ($t = 0.1-500 \ \mu s$). As detected in several previous studies [7, 29, 30], the slope of the distribution function for $v = 0,1$ is much greater compared to $v = 2-8$, indicating that the 'first level' N_2 vibrational temperature, $T_{0,1} = \frac{E_{01}}{\ln(n_0 / n_1)}$, where E_{01} is the energy difference between vibrational levels $v = 1$ and $v = 0$, and n_1 and n_0 are their populations, is much less compared to $T_{0,v}$ ($v = 2-8$). This effect, reproduced by the model, is due to the fact that the electron temperature in the pulsed discharge exceeds considerably the vibrational mode temperature. Therefore electron impact produces vibrational level populations $v > 1$ with the slope close to the electron temperature, much higher than the 'first level' vibrational temperature. A secondary 'kink' in the predicted vibrational distributions in figure 5, at $v = 4$, is due to vibrational excitation of the ground electronic state in energy pooling reaction (R2) (see table 1), since the present model assumes that only these two vibrational levels are populated during these processes.

Figure 6, which plots experimental and predicted $N_2(X \ ^1\Sigma_g^+, v = 0-9)$ populations versus time shows that the model underpredicts significant transient rise of vibrational level populations on a ~1–10 μs time scale. In our previous work [10], as well as in earlier work [29], it was suggested that this rise may be caused by significant ground state vibrational excitation in energy pooling processes, such as reactions (R1) and (R2). The present more accurate model predictions, however, show that this effect appears to be insufficient to interpret the data. Moreover, incorporating relatively modest energy addition by the after-pulse discharge (about 8.5% of the main discharge pulse, see figure 2) into the model suggests that it

may in fact produce noticeable additional vibrational excitation of the plasma, as illustrated in figure 7. Indeed, adding the after-pulse discharge filament with the diameter of 0.67 mm, generated at $t = 500$ ns, results in a significant jump of predicted vibrational level populations, such that they match their peak values measured in the afterglow (see figure 7). This occurs for two reasons, (i) smaller diameter of the partially constricted after-pulse filament compared to the main discharge pulse filament, producing higher specific energy loading, and (ii) considerably lower reduced electric field in the after-pulse discharge, resulting in higher discharge energy fraction going to vibrational excitation of ground electronic state N_2. Note, however, that the experimental results exhibit a gradual rise in vibrational level populations (see figure 7), rather than a sudden jump. This apparent discrepancy may be resolved by noticing that due to the small diameter of the after-pulse discharge filament, it may be not very reproducible pulse-to-pulse, and may well miss the laser beams for some laser shots during CARS signal accumulation, thus resulting in a more gradual signal rise. This possible artifact is discussed in greater detail at the end of section 3.

As shown in figure 8, temperature rise in the plasma on sub-microsecond time scale results in a noticeable pressure overshoot on the filament centerline, predicted by the model, by approximately 30%. Since the pressure rise occurs on sub-acoustic time scale, it generates a radial compression wave, which has been detected in nitrogen in our previous work [12].

In air, kinetics of energy thermalization and temperature rise during and after the discharge pulse becomes somewhat more complicated, as shown in figure 9. In this case, temperature in the plasma exhibits a well-pronounced two-stage rise, 'rapid' (sub-acoustic) heating on sub-μs time scale, and 'slow' heating on ~50–500 μs time scale. Kinetics of these two heating stages is discussed in detail in our previous work [5]. Basically, rapid heating occurs mainly in collisions of
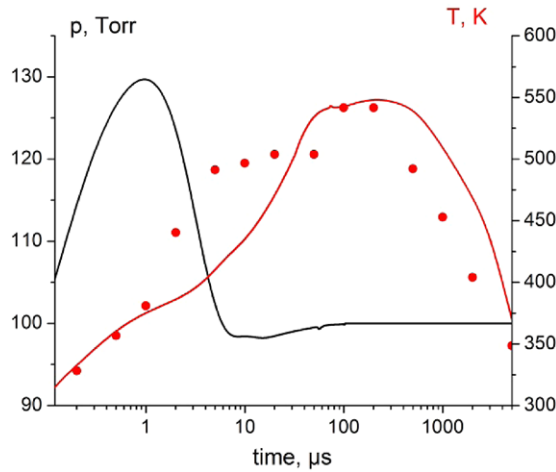
Figure 8. Time-resolved gas temperature (experimental and predicted) and pressure predicted on filament centerline during and after the discharge pulse in nitrogen. Symbols: experimental data, lines: model predictions.
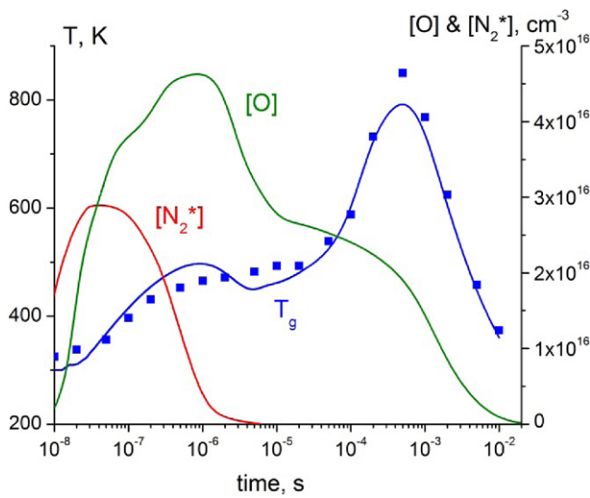
Figure 9. Time-resolved gas temperature (experimental and predicted), predicted number density of O atoms, and total number density of electronically excited states of N_2 and during and after the discharge pulse in air. Symbols: experimental data, lines: model predictions.

electronically excited nitrogen molecules with O_2, resulting in oxygen dissociation,

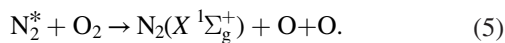$$N_2^* + O_2 \rightarrow N_2(X\ ^1\Sigma_g^+) + O + O. \tag{5}$$

Figure 9 shows that rapid temperature rise during and after the discharge pulse occurs on the same time scale as quenching of excited electronic states of nitrogen molecules by O_2, a few hundred nanoseconds. Gasdynamic expansion of the plasma filament, caused by its heating on sub-acoustic time scale, results in transient temperature reduction and O atom number density decrease, predicted by the model (see figure 9). Slow heating occurs during vibration–translation (V–T) relaxation of vibrationally excited N_2 by O atoms,

$$N_2(X\ ^1\Sigma_g^+, v) + O \rightarrow N_2(X\ ^1\Sigma_g^+, v-1) + O. \tag{6}$$
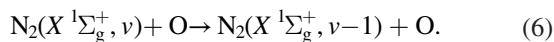
The time scale for the slow heating can be estimated from the net rate of V–T relaxation of nitrogen by O atoms, as was done
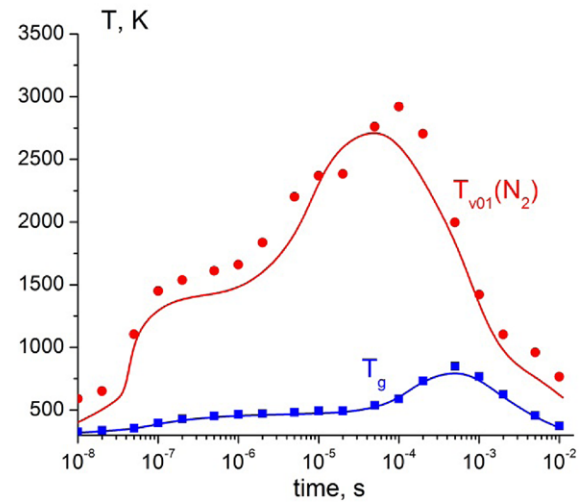
Figure 10. Experimental and predicted time-resolved gas temperature and 'first level' N_2 vibrational temperature during and after the discharge pulse in air. Symbols: experimental data, lines: model predictions.

in our previous work [5]. After peaking at $T \approx 850$ K, on the time scale of approximately 500 μs, the temperature decreases to near room temperature over about 10 ms due to radial diffusion, consistent with the model predictions (see figure 9).

Comparing the behavior of gas temperature with 'first level' N_2 vibrational temperature, $T_{0,1}$, plotted in figure 10, it can be seen that the 'slow' temperature rise begins at the same time when the vibrational temperature starts to decrease. N_2 vibrational temperature, which increases considerably during the main discharge pulse due to vibrational excitation by electron impact, continues to rise during the afterglow, on the time scale of a few tens of microseconds after the pulse, peaking at $T_{0,1} \approx 2900$ K, in good agreement with the model predictions (see figure 10). This effect, as discussed in greater detail in our previous work [5], is due to 'downward' V–V transfer in nitrogen with vibrational levels $v \geqslant 2$, strongly overpopulated by electron impact during the discharge,

$$N_2(v) + N_2(w=0) \rightarrow N_2(v-1) + N_2(w=1). \tag{7}$$
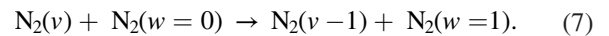
This process is illustrated further in figure 11, which compares experimental and predicted $N_2(v=0-8)$ vibrational level populations at different time delays after the discharge pulse. It can be seen that a 'kink' in the vibrational distribution function at $v=1$, generated during the discharge, gradually disappears at longer delay times, before V–T relaxation by O atoms reduces high vibrational level populations. Comparing figures 5 and 11, it is apparent that the 'straightening' of the vibrational distribution caused by the downward V–V energy transfer of equation (7) occurs in a similar way both in N_2 and air, as expected. On the other hand, V–T relaxation in air occurs much faster compared to nitrogen, due to rapid relaxation by O atoms. Figure 12, which plots N_2 vibrational level populations versus time, also illustrates transient rise of $N_2(v=0-4)$ populations after the discharge pulse due to this effect, in good agreement with the modeling predictions. Incorporating energy addition by a weak after-pulse shown in figure 3 results in additional vibrational excitation
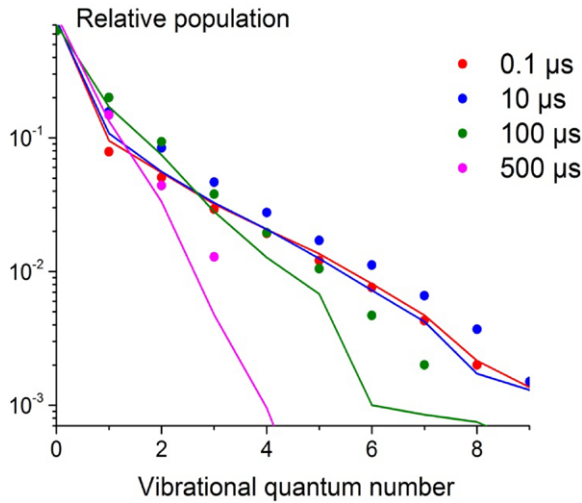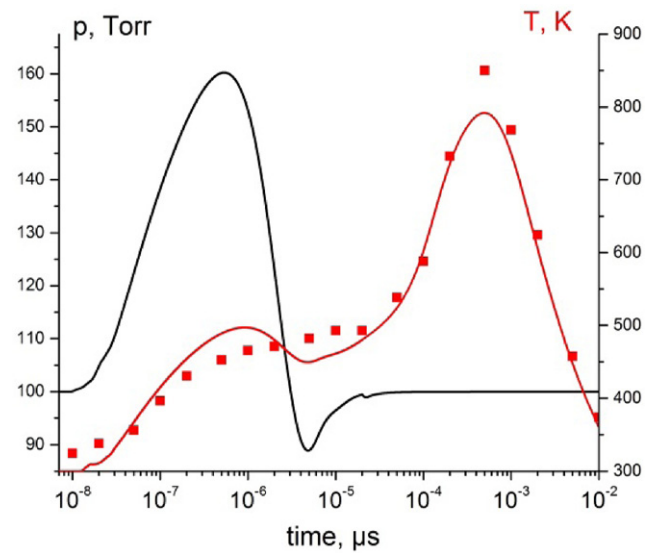
Figure 11. Experimental and predicted N_2 vibrational distribution functions after the discharge pulse in air, at different delay times after beginning of the main pulse. Symbols: experimental data, lines: model predictions.
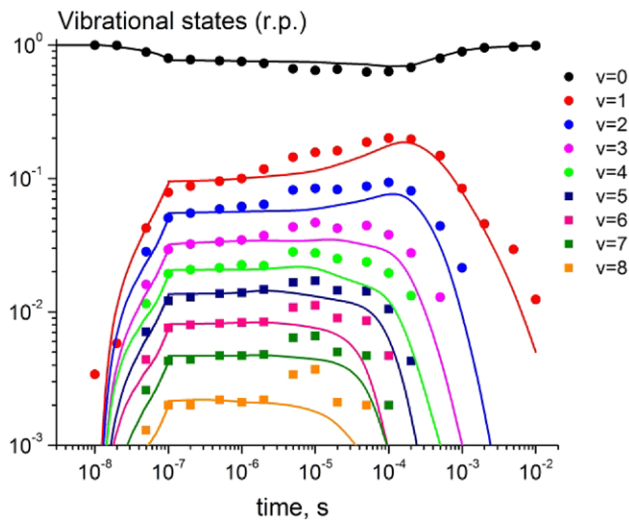

Figure 12. Experimental and predicted $N_2(v = 0–9)$ vibrational level populations, plotted versus time after beginning of the main discharge pulse in air. Symbols: experimental data, lines: model predictions.

Figure 13. Time-resolved gas temperature (experimental and predicted) and pressure predicted on filament centerline during and after the discharge pulse in air. Symbols: experimental data, lines: model predictions.
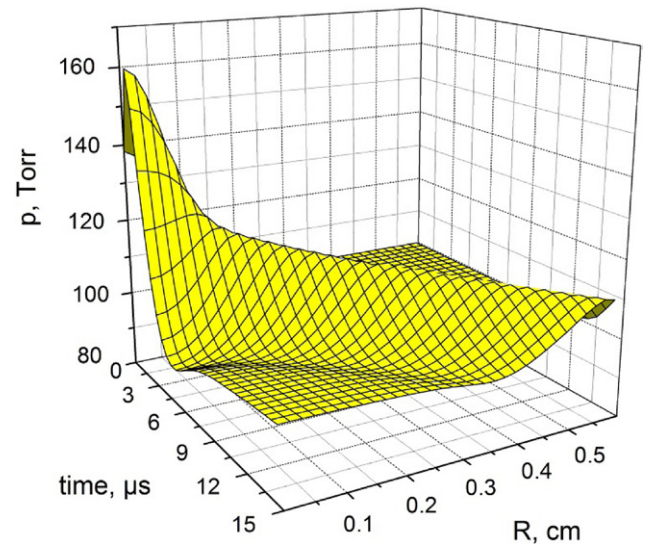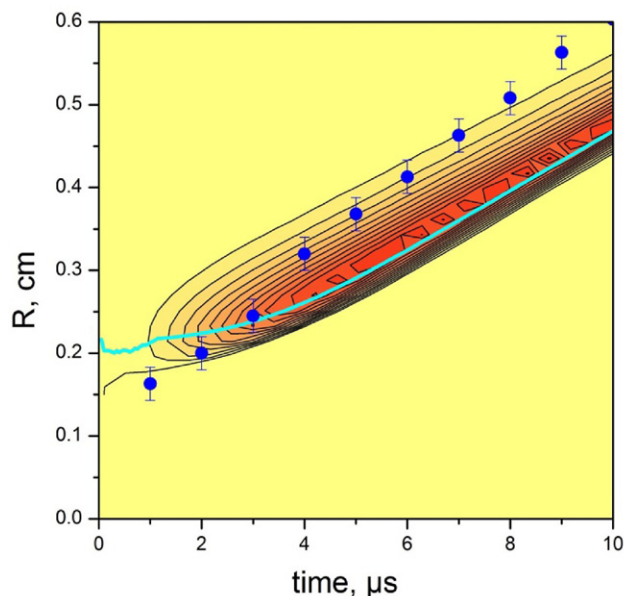

Figure 14. 3D contour plot of pressure distribution after the discharge pulse in air, plotted versus time delay after the pulse and radial distance.

of the plasma, although this effect is not as pronounced as in nitrogen (see figure 7). The difference between air and nitrogen is mainly due to a somewhat higher reduced electric field in the after-pulse plasma filament in air, compared to nitrogen, which reduces energy fraction into vibrational excitation of N_2 in the after-pulse.

Returning to discussion of temperature rise kinetics in air plasma, figure 13 shows that, as expected, 'rapid' near constant volume heating on sub-acoustic time scale, $t < \tau_{acoustic}$ ~ 3 μs, results in a significant pressure overshoot in the discharge filament, by about 60%. The pressure rise is considerably more pronounced than in nitrogen (see figure 8), due to higher rate of temperature rise in air, by approximately a factor of 2 ($\Delta T \approx 200$ K over 1 μs). After the overshoot, the discharge filament begins to expand and a compression wave propagates in the radial direction (see figure 14), causing rapid

pressure fall on the centerline and slight transient rarefaction to $P \approx 90$ Torr, before returning to baseline pressure.

Figure 15 compares time-resolved locations of the radial compression wave, obtained from phase-locked Schlieren images in our previous work [12], with the wave front location predicted by the present model (defined as the location of density gradient maximum). In the experiment, wave locations were determined from Schlieren frames taken after the discharge pulse 1 μs apart ($t = 0$ corresponds to the beginning of the main discharge pulse). It can be seen that the compression wave speed measured in the experiment is significantly higher compared to the model predictions. Average wave speed, determined as a slope to the trajectory at $r = 4–10$ mm, is 500 m s^{-1} in the experiment versus 360 m s^{-1} in the calculations.

Figure 15. Contour plot of pressure gradient distribution after the discharge pulse in air, showing predicted compression wave trajectory (blue line), compared with experimental wave trajectory (symbols).

This discrepancy cannot be explained by preheating of the gas by previous discharge pulses (e.g. see figure 13, which shows that the temperature on the filament centerline in the beginning of the discharge pulse only slightly exceeds the room temperature, by ~20–30 K. Variation of the discharge filament diameter by $\pm20\%$, which may be caused by the filament 'jitter' (transverse movement pulse-to-pulse) affected the wave speed only insignificantly, approximately by 5%. It is possible that the wave speed may be affected by interaction of the cylindrical compression wave generated by the discharge filament and the spherical compression wave originated in the cathode layer of the discharge [12], but verifying this conjecture requires exercising a 2D axisymmetric discharge/afterglow model.

The present kinetic model has also been used to analyze one of the puzzling results of experiments [10], which suggested that the total number of vibrational quanta per N_2 molecule continues increasing after the discharge pulse (on the time scale of ~1–100 μs), both in nitrogen and in air. In nitrogen, this effect, also detected in previous CARS measurements in a pulsed dc discharge in N_2 [29], may be interpreted as energy addition to the ground state vibrational model during collisional quenching of excited electronic states [10, 29]. However, in air this explanation becomes far less likely since electronically excited levels of nitrogen in air are quenched on a much shorter time scale, ~ 1 μs (see figure 9). The results of the present work suggest that this effect may be caused by a combination of discharge filament jitter and gasdynamic expansion caused by rapid heating. This effect is illustrated qualitatively in figure 16. Basically, transverse motion of the filament (in the direction perpendicular to the laser beams) results in a reduction of the CARS signal generated when the filament is displaced laterally, such that the laser beams probe its less excited, peripheral region (see

figure 16(a)). This effect is more pronounced at short delays after the discharge pulse, when gasdynamic expansion has not yet occurred, and the filament diameter is relatively small. However, as the filament expands and its diameter increases, the effect of its lateral movement on the CARS signal intensity would be less pronounced, since now the laser beams are predominantly probing a stronger excited near-axial region of the filament (see figure 16(b)). This effect would be interpreted as a rise of high vibrational level populations at long time delays after the discharge pulse, i.e. an apparent increase of the number of vibrational quanta per N_2 molecule. Lateral jitter of the main discharge filament may also cause the partially constricted after-pulse filament to miss the laser beams, as discussed above.

To estimate the significance of this effect on the number of quanta per molecule at the present conditions, the filament jitter was modeled as random transverse motion of the region 'probed' by the laser (with the amplitude of 0.2 mm), sampling N_2 vibrational level populations at different radial locations of the filament, and averaging the results for different delay times after the discharge pulse. The results of this semiqualitative estimate are shown in figure 17. It can be seen that random radial jitter of the expanding filament results in an apparent rise of vibrational quanta per N_2 molecule by ~20% on the time scale of ~ 5 μs, close to the experimental result of ~30% increase on the same time scale [10]. This result suggests that the effect of apparent rise of vibrational quanta per molecule is caused by the jitter and gasdynamic expansion of the filament, rather than by collisional energy transfer among different molecular energy modes.

At the present conditions, discharge energy fraction coupled to the positive column of the discharge filament in air is approximately 50%, with the rest coupled to the cathode layer. Significant energy coupling to the cathode layer of the discharge is apparent from Schlieren images taken in the afterglow, which indicate an additional compression wave originating from the surface of the cathode [12]. This demonstrates the importance of self-consistent modeling of the cathode layer of the discharge, in 2D geometry, for realistic prediction of the amplitude and shape of pressure perturbations produced by the discharge pulse. By the end of the discharge pulse in air, at t = 100 ns, approximately 50% of the energy coupled to the positive column is stored in the vibrational mode of ground electronic state N_2, 25% remains in electronically excited N_2^*, 15% goes to O_2 dissociation (both by electron impact and by quenching of N_2^*), and 10% is thermalized during N_2^* quenching by O_2. These energy fractions represent 25%, 12.5%, 7.5%, and 5% of the total discharge pulse energy, respectively. By the end of the pressure overshoot (i.e. before gasdynamic expansion), at $t = 1$ μs, positive column energy fractions stored in N_2 vibrational and electronic energy modes are 50% and 2–3% (i.e. 25% and 1%–2% of the total pulse energy), respectively, energy fraction stored in O atoms remains about 15% (7.5% of the total pulse energy), and thermalized energy increases to 20% (10% of the total pulse energy). Finally, energy stored in N_2 vibrational mode and O atoms is thermalized on the long time scale, t ~ 50–500 μs, without producing finite amplitude compression waves, and
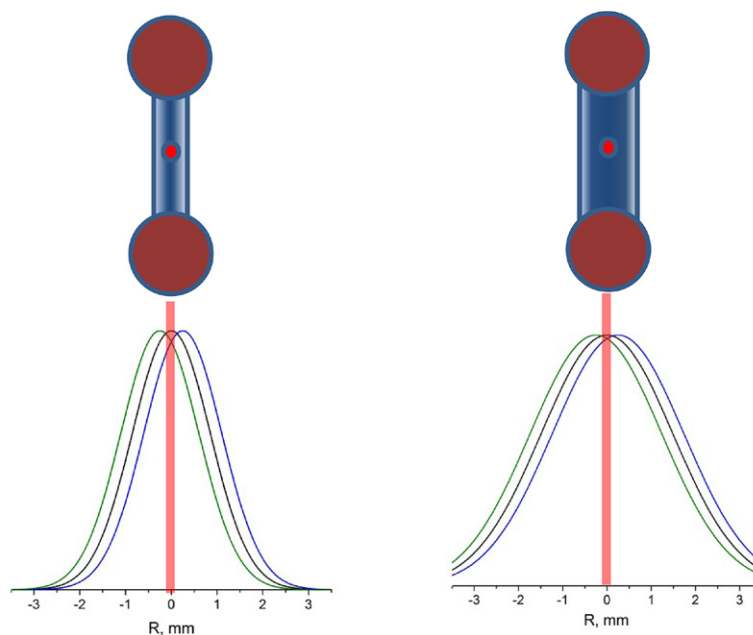
Figure 16. Cartoon schematic illustrating the effect of discharge filament 'jitter' on CARS signal collection: left, at short times delays (before gasdynamic expansion), and right, at long time delays (after the expansion) after the discharge pulse. The red dot and the red bar indicate the location of the overlapped laser beams, estimated to be ~100 μm in diameter. The curves illustrate Gaussian radial distributions of N_2 vibrational temperature, with FWHM of 2.0 mm (left) and 4.0 mm (right), displaced over ± 200 μm in the transverse direction.
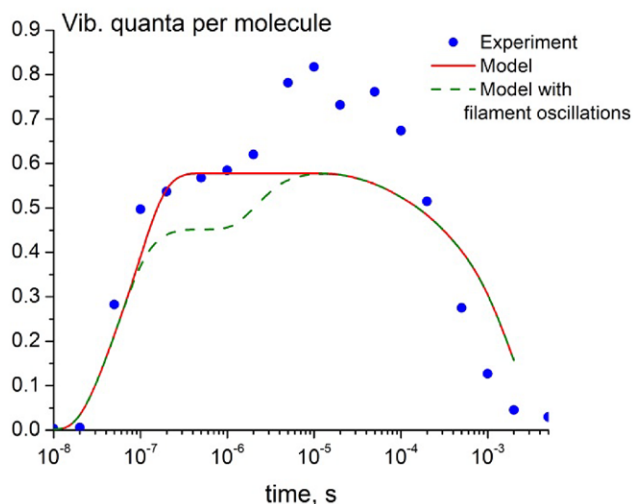
Figure 17. Comparison of experimental (symbols) and predicted (lines) time-resolved vibrational quanta per N_2 molecule in air, calculated with and without taking into account discharge filament 'jitter'.

diffuses out of the filament. Thus, it can be seen that at the present conditions, about 7.5% of the total discharge pulse energy is spend on O atom generation, and only about 10% is thermalized on sub-acoustic time scale.

5. Summary

In the present work, kinetic modeling is used to analyze energy partition and energy transfer in nanosecond pulse discharges in air and nitrogen. The modeling predictions are compared with time-resolved temperature and $N_2(v = 0–9)$ vibrational population measurements by picosecond broadband coherent anti-Stokes Raman spectroscopy (CARS) [10] and phase-locked Schlieren images of a compression wave generated due to heating of the discharge filament on sub-acoustic time scale [12]. The present kinetic model has been previously validated using time-resolved measurements of $N_2(v = 0–4)$ vibrational level populations, [N], [O], and [NO] in nanosecond pulse discharge in air at a lower specific energy loading [6], as well as time- and spatially resolved temperature measurements in nanosecond pulse discharges in air and H_2–air at a lower pressure [5].

In the experiments [10, 12] modeled in the present work, the diffuse filament, nanosecond pulse discharge (pulse duration ~100 ns) was sustained between two spherical electrodes at $P = 100$ torr and operated at a low pulse repetition rate, 50 Hz, to enable rotational–translational temperature and N_2 vibrational level population measurements over a wide range of time scales after the discharge pulse, from tens of ns to tens of ms. The present analysis is based on a 1D axial model for the discharge pulse, and a 1D radial axisymmetric model for the afterglow. The model shows good agreement with the experimental data, reproducing experimental discharge current pulse waveforms, as well as dominant processes of energy partition and energy transfer in the discharge and the afterglow. Specifically, the results demonstrate that energy thermalization and temperature rise occurs in two stages, (i) 'rapid' heating, occurring on the time scale τ_{rapid} ~ 0.1–3 μs (in nitrogen) and τ_{rapid} ~ 0.1–1 μs (in air), dominated by $N_2(A\ ^3\Sigma_u^+)$ energy pooling processes, $N_2(B^3\Pi_g)$ and $N(^2P,^2D)$ quenching (in nitrogen), and by quenching of multiple excited electronic states of N_2 molecules by O_2 (in air), and (ii) 'slow' heating, on the time scale τ_{slow} ~ 50–500 μs, caused primarily by N_2 vibrational relaxation by O atoms (in air), and nearly completely missing in nitrogen due to the much slower

vibrational relaxation rate. The results in air are consistent with our previous work [5].

Comparison of the model predictions with high spatial resolution measurements of $N_2(v = 0$–$9)$ vibrational level populations confirms the conclusions of our previous work [5, 24], which suggested that N_2 'first level' vibrational temperature rise after the discharge pulse is caused by the 'downward' vibrational–vibrational exchange depopulating higher vibrational levels and populating vibrational level $v = 1$. The model accurately reproduces temporal dynamics of vibrational level populations and temperature in the discharge and the afterglow. Thus, the present work provides experimental validation of the modeling predictions, based on accurate time-resolved temperature and $N_2(v = 0$–$9)$ population measurements. Rapid heating of the filament on sub-acoustic time scale produces a strong compression wave propagating in the radial direction, predicted by the present kinetic model and detected in previous experiments in nanosecond pulse filament discharges [11, 12]. The experimental wave speed is considerably higher compared to the model predictions, by approximately 30%. The reason for this discrepancy is not fully understood, and may be due to interaction between the cylindrical and spherical compression waves generated by the discharge filament and the cathode layer, respectively.

Since current in the cathode layer is dominated by the ion current, nearly all energy coupled to the cathode layer is thermalized extremely rapidly in ion-neutral collisions, both elastic and charge transfer. This occurs on the time scale of discharge pulse duration, ~100 ns, resulting in rapid temperature and pressure increase in the cathode layer. However, since the present 1D model does not account for a significantly larger surface area occupied by the cathode layer on the electrode, compared to the discharge filament cross sectional area (see figure 3), peak temperature and pressure values in the cathode layer predicted by the model may well be overpredicted. Predictive analysis of cathode layer kinetics requires the use of a full 2D model of the discharge.

Parametric modeling calculations for different voltage pulse waveforms demonstrated that, as expected, discharge energy fraction going into electronic excitation of nitrogen molecules increases with pulse peak voltage and decreases with voltage rise time. Basically, this suggests that increasing the discharge energy fraction thermalized during 'rapid heating' requires the use of short rise time, high peak voltage pulses. Similarly, since the dominant 'rapid heating' process of equation (5) in air results in effective generation of O atoms, similar pulse waveforms (i.e. short rise time, high peak voltage) are likely to be more effective for plasma assisted combustion applications. Finally, the effect of 'slow heating' driven by vibrational relaxation on flow perturbations is not fully understood, and further experiments in near-surface nanosecond pulse discharges are necessary to provide quantitative insight into this issue.

Acknowledgments

References

[1] Messina D, Attal B-T and Grisch F 2007 Study of a non-equilibrium pulsed nanosecond discharge at atmospheric pressure using coherent anti-Stokes Raman scattering *Proc. Combust. Inst.* **31** 825–32

[2] Stancu G D, Kaddouri F, Lacoste D A and Laux C O 2010 Atmospheric pressure plasma diagnostics by OES, CRDS and TALIF *J. Phys. D: Appl. Phys.* **43** 124002

[3] Rusterholtz D L, Lacoste D A, Stancu G D, Pai D Z and Laux C O 2013 Ultrafast heating and oxygen dissociation in atmospheric pressure air by nanosecond repetitively pulsed discharges *J. Phys. D: Appl. Phys.* **46** 464010

[4] Mintoussov E I, Pendleton S J, Gerbault F G, Popov N A and Starikovskaia S M 2011 Fast gas heating in nitrogen–oxygen discharge plasma: II. Energy exchange in the afterglow of a volume nanosecond discharge at moderate pressures *J. Phys. D: Appl. Phys.* **44** 285202

[5] Lanier S, Shkurenkov I, Adamovich I V and Lempert W R 2015 Two-stage energy thermalization mechanism in nanosecond pulse discharges in air and hydrogen–air mixtures *Plasma Sources Sci. Technol.* **24** 025005

[6] Burnette D, Montello A, Adamovich I V and Lempert W R 2014 Nitric oxide kinetics in the afterglow of a diffuse plasma filament *Plasma Sources Sci. Technol.* **23** 045007

[7] Lo A, Cléon G, Vervisch P and Cessou A 2012 Spontaneous Raman scattering: a useful tool for investigating the afterglow of nanosecond scale discharges in air *Appl. Phys.* B **107** 229

[8] Lo A, Cessou A, Boubert P and Vervisch P 2014 Space and time analysis of the nanosecond scale discharges in atmospheric pressure air: I. Gas temperature and vibrational distribution function of N_2 and O_2 *J. Phys. D: Appl. Phys.* **47** 115201

[9] Lo A, Cessou A and Vervisch P 2014 Space and time analysis of the nanosecond scale discharges in atmospheric pressure air: II. Energy transfers during the post-discharge *J. Phys. D: Appl. Phys.* **47** 115202

[10] Montello A, Yin Z, Burnette D, Adamovich I V and Lempert W R 2013 Picosecond CARS measurements of nitrogen vibrational loading and rotational/translational temperature in nonequilibrium discharges *J. Phys. D: Appl. Phys.* **46** 464002

[11] Xu D A, Lacoste D A, Rusterholtz D L, Elias P-Q, Stancu G D and Laux C O 2011 Experimental study of the hydrodynamic expansion following a nanosecond repetitively pulsed discharge in air *Appl. Phys. Lett.* **99** 121502

[12] Montello A, Burnette D, Nishihara M, Lempert W R and Adamovich I V 2013 Dynamics of rapid localized heating in nanosecond pulse discharges for high speed flow control *J. Fluid Sci. Technol.* **8** 147–59

[13] Roupassov D V, Nikipelov A A, Nudnova M M and Starikovskii A Yu 2009 Flow separation control by plasma actuator with nanosecond pulsed-periodic discharge *AIAA J.* **47** 168

[14] Little J, Takashima K, Nishihara M, Adamovich I and Samimy M 2012 Separation control with nanosecond pulse driven dielectric barrier discharge plasma actuators *AIAA J.* **50** 350–65

[15] Ju Y and Sun W 2015 Plasma assisted combustion: dynamics and chemistry *Prog. Energy Combust. Sci.* **48** 21–83

[16] Graves D B 2012 The emerging role of reactive oxygen and nitrogen species in redox biology and some implications for plasma applications to medicine and biology *J. Phys. D: Appl. Phys.* **45** 263001

[17] Popov N A 2001 Investigation of the mechanism for rapid heating of nitrogen and air in gas discharges *Plasma Phys. Rep.* **27** 886

[18] Popov N A 2011 Fast gas heating in a nitrogen-oxygen discharge plasma: I. Kinetic mechanism, *J. Phys. D: Appl. Phys.* **44** 285201

[19] Marode E, Djermoune D, Dessante P, Deniset C, Segur P, Bastien F, Bourdon A and Laux C 2009 Physics and applications of atmospheric non-thermal air plasma with reference to environment *Plasma Phys. Control. Fusion* **51** 124002

[20] Tholin F and Bourdon A 2011 Influence of temperature on the glow regime of a discharge in air at atmospheric pressure between two point electrodes *J. Phys. D: Appl. Phys.* **44** 385203

[21] Tholin F and Bourdon A 2013 Simulation of the hydrodynamic expansion following a nanosecond pulsed spark discharge in air at atmospheric pressure *J. Phys. D: Appl. Phys.* **46** 365205

[22] Nagaraja S, Yang V and Adamovich I 2013 Multi-scale modeling of pulsed nanosecond dielectric barrier plasma discharges in plane-to-plane geometry *J. Phys. D: Appl. Phys.* **46** 155205

[23] Takana H and Nishiyama H 2014 Numerical simulation of nanosecond pulsed DBD in lean methane-air mixture for typical conditions in internal engines *Plasma Sources Sci. Technol.* **23** 034001

[24] Shkurenkov I, Burnette D, Lempert W R and Adamovich I V 2014 Kinetics of excited states and radicals in a nanosecond pulse discharge and afterglow in nitrogen and air *Plasma Sources Sci. Technol.* **23** 065003

[25] Guerra V, Sá P A and Loureiro J 2004 Kinetic modeling of low-pressure nitrogen discharges and post-discharges *Eur. Phys. J. Appl. Phys.* **28** 125–52

[26] Popov N A 2013 Vibrational kinetics of electronically-excited $N_2(A\,^3\Sigma_u^+, v)$ molecules in nitrogen discharge plasma *J. Phys. D: Appl. Phys.* **46** 355204

[27] Herron J T 1999 Evaluated chemical kinetics data for reactions of $N(^2D)$, $N(^2P)$, and $N_2(A\,^3\Sigma_u^+)$ in the gas phase *J. Phys. Chem. Ref. Data* **28** 1453–83

[28] Galvao B R L, Braga J P, Belchior J C and Varandas A J C 2014 Electronic quenching in $N(^2D) + N_2$ collisions: a state-specific analysis via surface hopping dynamics *J. Chem. Theory Comput.* **10** 1872–7

[29] Devyatov A A, Dolenko S A, Rakhimov A T, Rakhimova T V, Roi N N and Suetin N V 1986 Investigation of kinetic processes in molecular nitrogen by the CARS method *Sov. Phys.—JETP* **63** 246–50

[30] Vereshchagin K A, Smirnov V V and Shakhatov V A 1997 CARS study of the vibrational kinetics of nitrogen molecules in the burning and afterglow stages of a pulsed discharge *Tech. Phys.* **42** 487–94